

# Anyonic defect braiding and spontaneous chiral symmetry breaking in dihedral liquid crystals

Alexander Mietke\* and Jörn Dunkel†

*Department of Mathematics, Massachusetts Institute of Technology,  
77 Massachusetts Avenue, Cambridge, Massachusetts 02139-4307, USA*

Dihedral ( $k$ -atic) liquid crystals (DLCs) are assemblies of microscopic constituent particles that exhibit  $k$ -fold discrete rotational and reflection symmetries. Generalizing the half-integer defects in nematic liquid crystals, two-dimensional  $k$ -atic DLCs can host point defects of fractional topological charge  $\pm m/k$ . Starting from a generic microscopic model, we derive a unified hydrodynamic description of DLCs with aligning or anti-aligning short-range interactions in terms of Ginzburg-Landau and Swift-Hohenberg theories for a universal complex order-parameter field. Building on this framework, we demonstrate in both continuum and particle simulations how adiabatic braiding protocols, implemented through suitable boundary conditions, can emulate anyonic exchange behavior in a classical system. The theory further predicts a novel spontaneous chiral symmetry breaking transition in anti-aligning DLCs, in quantitative agreement with particle simulations.

## I. INTRODUCTION

Microscopic particle symmetries fundamentally determine the macroscopic order and dynamics of liquid and crystalline phases of matter [1, 2]. Recent technological and experimental progress [3–5] enables unprecedented precise control over the fabrication and assembly of nanoparticles [6, 7] and polyhedral colloids [8–12] with tunable interactions [9, 13–15]. These advances have led to a renewed theoretical and computational interest in  $k$ -atic dihedral liquid crystals (DLCs) with discrete  $k$ -fold rotational and reflection symmetries [16–22]. Going beyond the widely investigated polar ( $k = 1$ ) and nematic ( $k = 2$ ) liquid crystals [1], recent studies showed that assemblies of triatic [19] ( $k = 3$ ) and higher-order polyhedral [18] objects ( $k \geq 3$ ) can exhibit striking symmetry breaking phenomena. Furthermore, thanks to seminal work by de Gennes [23], Halperin and Lubensky [24], and others [25–28], it is well-known that the phenomenological description of 2D liquid crystals shares interesting mathematical similarities [29] with superconductors. Despite their fundamental microscopic differences, both classes of systems can at the mean-field level be described by a complex field  $\Psi(t, \mathbf{r}) = |\Psi|e^{i\phi}$  whose magnitude  $|\Psi|$  and phase  $\phi(t, \mathbf{r})$  encode local order.

A remarkable characteristic of two-dimensional (2D) DLCs is their ability to host point defects of fractional topological charge [19, 28], similar to anyonic quasiparticle excitations in 2D quantum matter [30, 31]. One of the defining features of anyonic excitations is the behavior of their wave function under pair exchange: When two identical anyons with initial positions  $\mathbf{r}_1$  and  $\mathbf{r}_2$  are braided counterclockwise around each other, their complex wave function  $\psi$  changes according to  $\psi(\mathbf{r}_2, \mathbf{r}_1) = e^{i2\pi/k}\psi(\mathbf{r}_1, \mathbf{r}_2)$ , where  $k = 1, 2, \dots$ . That is, anyonic wave functions acquire a phase  $\theta = 2\pi/k$  under particle exchange; bosons and fermions correspond to the special cases  $k = 1$  and  $k = 2$ , respectively. First predicted [32] in 1977 and named [30] in 1982, anyons played an im-

portant role in the theoretical explanation of the fractional quantized Hall effect [33–35]. More recently, they have been intensely explored in the context of topological quantum computing [36, 37], and two recent experimental studies [38, 39] reported first direct evidence for anyonic quantum statistics. From a general theoretical perspective, the mathematical parallels between the mean-field descriptions of 2D liquid crystals and 2D quantum systems raise the interesting question whether or not one can emulate anyonic exchange symmetries in suitably designed liquid crystal systems.

Here, we will show that it is indeed possible to create, stabilize and manipulate fractional defect-pair configurations  $(\mathbf{r}_1, \mathbf{r}_2)$  in  $k$ -atic DLCs, such that the order parameter field  $\Psi(t, \mathbf{r}; \mathbf{r}_1, \mathbf{r}_2)$  transforms globally as  $\Psi(t, \mathbf{r}; \mathbf{r}_2, \mathbf{r}_1) = e^{i2\pi/k}\Psi(t, \mathbf{r}; \mathbf{r}_1, \mathbf{r}_2)$  when the two defects are braided around each other. To this end, we first derive a hydrodynamic mean-field description of DLCs by starting from a generic  $XY$ -type particle interaction model on a random lattice. We then verify that the derived mean-field theory agrees quantitatively with simulations of the particle model. After this validation step, we demonstrate explicitly in both continuum and particle simulations how adiabatically modulated boundary anchoring conditions can be used to implement anyonic defect braiding protocols in DLC systems. Finally, we identify a novel chiral symmetry breaking transition in classical DLCs with anti-aligning short-range interactions, which manifests itself through the spontaneous formation of stable braidable spiral patterns in the phase angle fields. The close agreement between mean-field theory and particle simulations suggests that the theoretical predictions presented below could be realized with 3-fold symmetric molecules, such as 1,3,5-trichlorobenzene [19] or DNA-origami structures [40–42], or polyhedral [4, 18], magnetic [43] and DNA-coated colloids [8, 44].

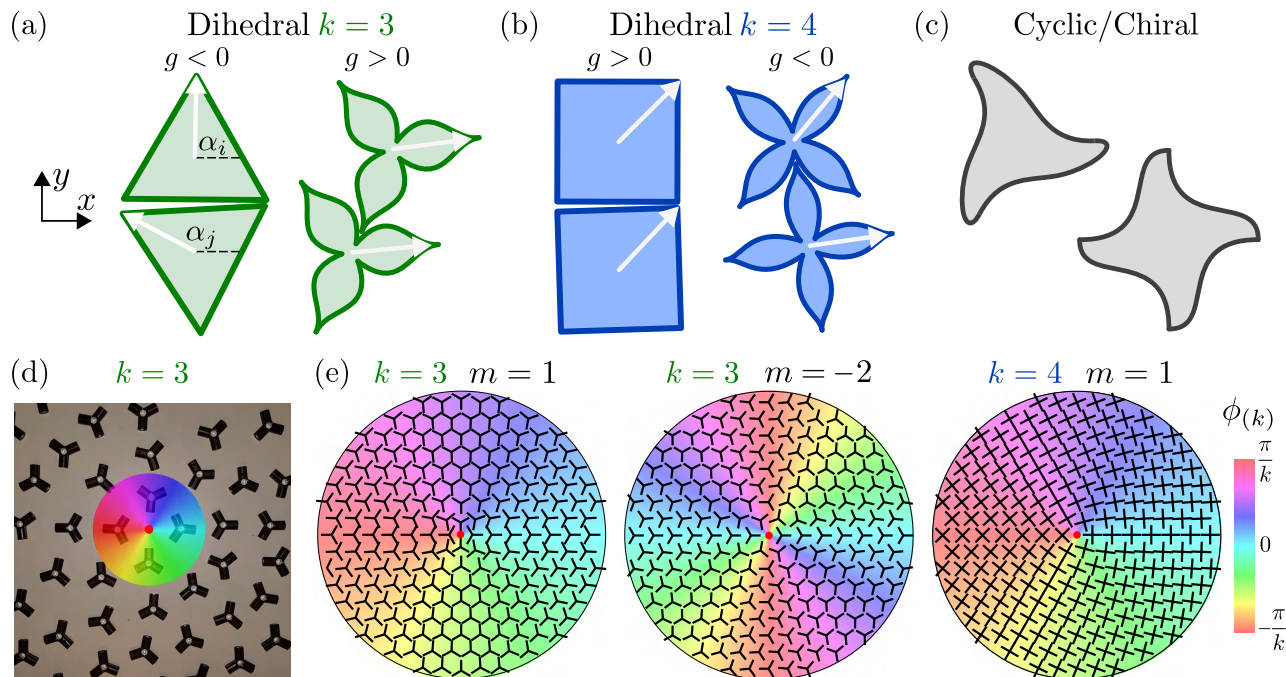


FIG. 1. Illustration of DLC particles,  $k$ -atic order and point defects carrying fractional topological charges  $m/k$ . (a,b) Examples of 3-atic ( $k = 3$ ) and 4-atic ( $k = 4$ ) dihedral particles with aligning ( $g > 0$ ) and anti-aligning ( $g < 0$ ) interactions. Director vectors are shown as white arrows. (c) Examples of chiral non-DLC particles that exhibit  $k$ -fold rotational (cyclic) symmetry but lack reflection symmetry. The present study focusses exclusively on dihedral particles as in panels (a) and (b). (d) Realization of a  $+1/3$ -defect in collection of 3-legged symmetric LEGO connectors with mutually repulsive magnetic interactions. (e) From left to right:  $k$ -atic phase angle fields  $\phi(k)$  for point defects of topological charge  $+1/3$  in a 3-atic ( $k = 3, m = 1$ ), charge  $-2/3$  in a 3-atic ( $k = 3, m = -2$ ) and charge  $+1/4$  in a 4-atic field ( $k = 4, m = 1$ ) with local  $k$ -atic directors overlaid.

## II. MEAN-FIELD DESCRIPTION OF 2D DLCs WITH ALIGNING AND ANTI-ALIGNING INTERACTIONS

Generalizations of polar and nematic liquid crystals to higher-order symmetry groups are often called  $k$ -atics [28], where the integer  $k$  counts the discrete rotational symmetries of the constituent particles (Fig. 1a,b). Here, we focus on systems of particles that have both  $k$ -fold discrete rotational and reflection symmetry (Fig. 1a,b). This set of symmetry transformation defines the dihedral group  $D_k$ , which maps a regular polygon with  $k$  corners onto itself. Accordingly, we will refer to such systems generically as dihedral liquid crystals (DLCs). Note that the invariance under reflections excludes chiral particles, which can still have discrete rotational (cyclic) symmetry (Fig. 1c). Depending on whether  $k$  is even or odd, and whether the effective particle shape is convex or concave, DLCs can have aligning or anti-aligning interactions (Fig. 1a,b). Here, ‘shape’ can be understood in a broader sense as the angular symmetry of the particle’s pair-interaction potential, for which we will provide specific examples in Sec. III. As we will show in detail below, monodisperse DLCs with aligning and anti-aligning interactions can be described by a single universal mean-field equation. Before delving into the more technical discussion, it is instructive to anticipate

the structure of the resulting mean-field equations and their relations to anyonic exchange symmetries.

### A. Universal mean-field equation

In the limit of a constant particle density, a unified mean-field description of 2D monodisperse DLCs can be given in terms of a complex-valued scalar order parameter field  $\Psi_k(t, \mathbf{r})$ , which is governed by

$$\tau \partial_t \Psi_k = - (A + B |\Psi_k|^2) \Psi_k + \mathcal{L} (\nabla^2) \Psi_k. \quad (1)$$

The magnitude  $|\Psi_k|$  characterizes the degree of local order (alignment) of the director unit vectors (white arrows in Fig. 1a,b), and the phase angle of  $\Psi_k$  their mean orientation. The subscript  $k$  indicates the  $k$ -fold symmetry, and  $\tau$  is a relaxation time-scale that can be computed from the microscopic particle dynamics. As shown in detail below, the real parameters  $A$  and  $B$  depend on the particle symmetry and interaction strength, and  $\mathcal{L}$  is a linear operator. For aligning interactions,  $\mathcal{L}$  reduces to a simple Laplacian  $\mathcal{L} = L^2 \nabla^2$ ; in this case, Eq. (1) corresponds a ‘real’ Ginzburg-Landau (GL) equation [45] with an effective diffusion constant  $D = L^2/\tau$  (Sec. IV). For anti-aligning interactions,  $\mathcal{L}$  will take the form of a pattern-forming Swift-Hohenberg-type (SH) [46] operator  $\mathcal{L} = -L_1^2 \nabla^2 - L_2^4 (\nabla^2)^2$  (Sec. V).

Conceptually, Eq. (1) formalizes the mathematical correspondence between the mean-field descriptions of DLCs and quantum fluids. If  $\tau$  in Eq. (1) is taken to be purely imaginary and  $\mathcal{L}$  is proportional to the Laplacian, then one recovers the Gross-Pitaevskii equation [47, 48]. The rhs. of Eq. (1) can be written as a functional derivative  $-\delta\mathcal{E}/\delta\Psi_k^*$ . For instance, when  $\mathcal{L} = L^2\nabla^2$ , the energy takes the form [28]

$$\mathcal{E} = \int d^2r \left( A|\Psi_k|^2 + \frac{B}{2}|\Psi_k|^4 + L^2|\nabla\Psi_k|^2 \right). \quad (2)$$

Thus, 2D DLCs and quantum fluids can be considered energetically equivalent at the mean-field level, while differing by the fact that the former have dissipative dynamics whereas the latter have conservative dynamics. Similar mean-field correspondences played a historically important role for the understanding of smectic liquid crystal phases by analogy with superconductors [23, 24, 27]. In the context of our present study, Eq. (1) provides the basis for realizing classical counterparts of anyon exchange symmetries. More specifically, we will see below that Eq. (1) accurately describes the formation, stability and decay (Figs. 2, 4), and the braiding (Figs. 3, 5) of fractional topological defects as observed in particle simulations of generic  $XY$ -type microscopic DLC models. When appropriately braided around each other, these fractional topological defects mimic the behavior of anyonic quasi-particle excitations, by acquiring a global phase-shift in the complex order parameter field.

### B. Fractional topological charges

To characterize the orientational order of DLCs, one can express the complex order-parameter field in the polar form (Appendix B 1)

$$\Psi_k = |\Psi_k|e^{ik\phi_{(k)}} \quad (3)$$

The magnitude field  $|\Psi_k|$  measures the strength of the local  $k$ -atic order, and the phase angle field

$$\phi_{(k)} = \frac{\arg \Psi_k}{k} \quad (4)$$

indicates the mean director orientation. The widely studied polar and nematic liquid crystals correspond to  $k = 1$  and  $k = 2$ , with microscopic constituents symmetric under rotations of  $2\pi$  or  $\pi$ , respectively.

The phase field  $\phi_{(k)}$  of a  $k$ -fold symmetric DLC can host commensurate fractional point defects (Appendix B 2). The net topological defect charge  $q$  enclosed by a positively oriented curve  $\mathcal{C}$  is obtained as

$$q = \frac{1}{2\pi} \oint_{\mathcal{C}} d\mathbf{l} \cdot \nabla\phi_{(k)} = \frac{m}{k}, \quad (5)$$

where  $m$  can be any integer. Examples of defect states for 3-atic and 4-atic DLCs are illustrated in Fig. 1d,e. The

‘experimental’ realization of  $+1/3$ -defect in Fig. 1d was assembled from 3-atic LEGO toy elements that are invariant under  $2\pi/3$ -rotations and corresponding reflections, and carry repulsive magnetic dipoles in each of their legs. Owing to the discrete symmetry of each microscopic element, only a rotation by  $2\pi/k$  is required before a particle returns to its initial configuration. If particle orientations along the integration contour complete  $|m|$  counterclockwise rotations in total then the defect charge is positive with  $m > 0$  in Eq. (5), whereas  $m < 0$  signals the completion of  $|m|$  clockwise  $2\pi/k$ -rotations along the curve  $\mathcal{C}$ .

### III. MICROSCOPIC DLC MODEL

*A priori*, it is not clear how well a mean-field model can capture the behavior of a specific microscopic DLC system. To validate predictions obtained from Eq. (1), we will compare them against simulations of a generic microscopic DLC model that can realize both aligning and anti-aligning interactions. Specifically, we consider an  $XY$ -type model [49] describing particles with local orientation angles  $\alpha_i(t) \in [0, 2\pi]$  that interact according to the overdamped dynamics

$$\frac{d\alpha_i}{dt} = \frac{g}{\pi R_\alpha^2} \sum_{j \in \mathcal{N}_i} \sin[k(\alpha_j - \alpha_i)] + \sqrt{2D_r}\xi_i(t). \quad (6)$$

Equation (6) is invariant under rotations  $\alpha_i \rightarrow \alpha_i + 2\pi/k$  and corresponding reflections along the symmetry axis of the particles. The parameter  $g$  sets the effective interaction strength between particle  $i$  and particles  $j$  in a neighborhood  $\mathcal{N}_i$  of radius  $R_\alpha$ . For  $g > 0$ , the  $k$ -atic directors of nearby particles tend to align, whereas  $g < 0$  favors anti-alignment (Fig. 1a,b). The Gaussian white noise  $\xi_i(t)$  has zero mean, satisfies  $\langle \xi_i(t)\xi_j(t') \rangle = \delta_{ij}\delta(t-t')$ , and  $D_r$  is the rotational diffusion constant. In all simulations presented below, particles were randomly placed inside a circular disk domain and given time to redistribute homogeneously through isotropic short-range repulsion (Appendix D 4). Thereafter, the particle positions were held fixed and the angular dynamics (6) was turned on. Equation (6) may thus be interpreted as a generalized classical  $XY$ -model on a densely packed random lattice [50].

#### A. Discrete $k$ -scaling invariance

In agreement with mean-field predictions, simulations for particles with  $k$ -fold symmetry show topological defects of fractional charges that are integer multiples of  $1/k$  (Fig. 2). We note, however, that for any value of  $k$ , the dynamics given in Eq. (6) can be mapped onto an equivalent polar model with  $k = 1$ , by defining rescaled director angles  $\alpha'_i = k\alpha_i$ , a rescaled alignment strength  $g' = gk$  and a rescaled rotational diffusion  $D'_r = D_r k^2$ . The fact that Eq. (6) can be rescaled in this

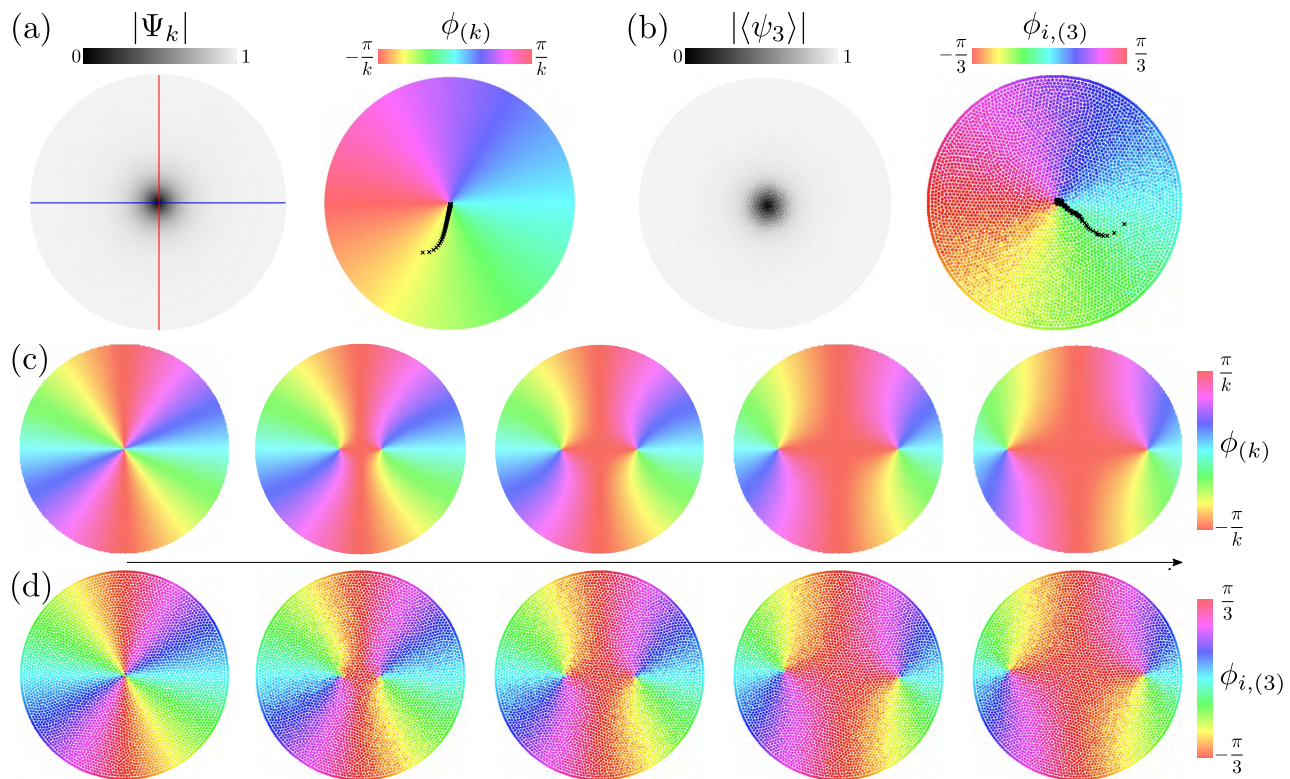


FIG. 2. Mean-field theory correctly predicts defect formation, stability and decay as seen in the particle model with aligning interactions ( $g > 0$ ) on a unit disk. (a) Stationary  $1/k$ -defect solution emerging from random initial conditions in the mean-field Eq. (1) with  $\mathcal{L} = L^2 \nabla^2$ ,  $A = -1$ ,  $B = 1$ ,  $L = 0.08$ , for boundary anchoring Eq. (14) with  $m = 1$  and  $\gamma_k = \theta$ . The lines  $\text{Re}\Psi_k = 0$  (red) and  $\text{Im}\Psi_k = 0$  (blue) indicate how the boundary anchoring induces a point defect with  $|\Psi_k| = 0$  inside the unit disk. The defect trajectory (black) shows that the defect appears at a random position in the bulk and subsequently moves towards the center of the disk (Movie 1). (b) Steady-state  $1/3$ -defect emerging from random initial conditions in particle simulations of Eq. (6) with  $k = 3$ , using the same boundary anchoring as in (a).  $\langle\psi_3\rangle$  denotes the time-average of the local 3-atic order parameter  $\psi_3 = \sum_{j \in \mathcal{N}_i} \exp(3i\alpha_j) / |\mathcal{N}_i|$  at steady state, and  $\phi_{i,(k)} = \arg(e^{ik\alpha_i}) / k$  is the instantaneous  $k$ -atic director orientation. In agreement with the mean-field prediction, the defect trajectory (black) shows that a phase defect forms at a random position in the bulk and moves stochastically towards the center of the disk (Movie 1). (c,d) For anchoring conditions  $\gamma_k = \theta$  and  $m = 2$ , a  $2/k$ -defect decays into two  $1/k$ -defects in both the mean-field simulations (c) and 3-atic particle simulations (d), see Movie 2. Snapshots show instantaneous phase fields at  $t/\tau \in \{0, 7.5, 15, 37.5, 150\}$  [Eq. (1); c] and  $t/\bar{\tau} \in \{0, 18, 36, 80, 320\}$  (particle model; d). Simulations of Eq. (6) used 4,000 non-anchored bulk particles, 900 boundary particles with fixed anchoring profile Eq. (17), and parameters  $D_r = 1$  (rotational diffusion chosen as characteristic time scale of particle simulations),  $R_\alpha = 0.2$  (interaction radius) and  $g = 0.25$  (interaction strength).

form essentially explains why the DLC particle models with different  $k$  can be described by the same mean-field Eq. (1). Although, as we will discuss next, the coefficients in Eq. (1) depend on  $k$ , the structure of the mean-field equation remains preserved for particles with different dihedral symmetries.

### B. Mean-field parameters

To show how Eq. (1) can be derived from the microscopic model in Eq. (6), we generalize standard coarse-graining procedures [51–53] to the case of  $k$ -atic particle interactions with a finite spatial range [54–56] (Appendix A). To this end, we decompose the one-particle probability density function of the  $N$ -particle system,

which is defined by the Gaussian white-noise average

$$f(\alpha, \mathbf{r}, t) = \sum_{i=1}^N \langle \delta(\alpha - \alpha_i(t)) \delta(\mathbf{r} - \mathbf{r}_i) \rangle, \quad (7)$$

into its angular moments

$$f_n(\mathbf{r}, t) = \int_0^{2\pi} d\alpha f(\alpha, \mathbf{r}, t) e^{in\alpha}. \quad (8)$$

The mode  $f_0$  represents the particle number density  $\rho$  of the system, which in our case is homogeneous and fixed. Accordingly, we define normalized and dimensionless modes by

$$\psi_n = \frac{f_n}{\rho}. \quad (9)$$

Equations (6) and (8) yield an infinite hierarchy of dynamic equations for the complex modes  $\psi_n$  (Appendix A). Despite being nonlinear, these equations decouple modes with  $n = jk$  for integers  $j \neq 0$  from all modes with  $n \neq jk$ , which can be understood as a consequence of the  $k$ -rescaling property of the microscopic model in Eq. (6). In the limit of a vanishing interaction radius  $R_\alpha \rightarrow 0$ , one then finds the spatially homogeneous dynamics (Appendix A 1)

$$\bar{\tau} \partial_t \psi_k = -(\bar{A} + \bar{B} |\psi_k|^2) \psi_k := F_k^{(0)}, \quad (10)$$

with characteristic relaxation time-scale  $\bar{\tau} = 2/(|g|k\rho)$  and parameters

$$\bar{A} = -\text{sgn}(g) \left(1 - \frac{2D_r k}{g\rho}\right), \quad \bar{B} = \frac{|g|\rho}{4D_r k}. \quad (11)$$

By comparing Eqs. (10) and (11) with Eq. (1), we can identify  $\psi_k \simeq \Psi_k$ ,  $\bar{\tau} \simeq \tau$ ,  $\bar{A} \simeq A$  and  $\bar{B} \simeq B$ , indicating that the particle dynamics (6) provides a microscopic realization of the mean-field theory (1). Below, we extend Eq. (10) to short-range interactions with  $R_\alpha > 0$ , which leads to leading-order corrections in the form of linear operators  $\mathcal{L}(\nabla^2)$ , corresponding to the second term on the rhs. of Eq. (1).

Beforehand, we note that Eq. (10) generalizes the corresponding result [52] for polar systems ( $k = 1$ ) to arbitrary  $k$ -atic systems. A change in the sign of the coefficient  $\bar{A}$  signals the spontaneous emergence of homogeneous  $k$ -atic order due to a linear instability of Eq. (10) if  $g > g^* := 2kD_r/\rho > 0$ , corresponding to an instability at wave vector  $\mathbf{q} = 0$ . This also implies that for anti-aligning interactions with  $g < 0$ , the disordered state is linearly stable in the limit of point-wise interactions.

In the remainder, we will consider the experimentally relevant case of systems with finite interaction range  $R_\alpha > 0$ . By comparing the mean-field predictions of Eq. (1) with quantitatively mapped microscopic models described by Eq. (6), we will demonstrate the controlled manipulation of fractional defects through boundary anchoring (Sec. IV) and the spontaneous formation of chiral textures (Sec. V).

#### IV. ANYONIC DEFECT BRAIDING IN ALIGNING DLCs ( $g > 0$ )

We first show that for aligning short-range interactions in the particle model Eq. (6), the mean-field description (1) takes the form of a real GL equation. Thereafter, we identify boundary anchoring conditions that will allow us to position and manipulate fractional defects in both mean-field and particle simulations. We will then apply this framework to implement the classical counterpart of an anyonic exchange symmetry, by braiding two identical point defects and observing a global phase change of  $\pi/k$  in their complex order-parameter field  $\Psi_k$ .

#### A. GL mean-field theory for aligning $k$ -atics

Assuming aligning interactions ( $g > 0$ ; Fig. 1a,b) and an isotropic interaction neighborhood in the particle model Eq. (6), the spatio-temporal  $k$ -atic mode dynamics can be approximated by (Appendix A 2)

$$\bar{\tau} \partial_t \psi_k(\mathbf{r}, t) \approx F_k^{(0)} + \frac{R_\alpha^2}{8} \nabla^2 \psi_k(\mathbf{r}, t), \quad (12)$$

with  $F_k^{(0)}$  given in Eq. (10). Note that the effective diffusion constant  $\bar{D} = R_\alpha^2/(8\bar{\tau})$  is not the result of actual particle diffusion but instead arises from the finite-range interactions between particles at fixed positions.

Equation (12) shows that the mean-field description of aligning DLC particle systems is given by Eq. (1) with

$$\mathcal{L} = L^2 \nabla^2, \quad L \simeq \frac{R_\alpha}{\sqrt{8}}, \quad (13)$$

corresponding to a ‘real’ GL equation [45] for the  $k$ -atic order parameter  $\Psi_k$ . The correlation length  $L$  is related to an effective bending rigidity that penalizes deviations of the  $k$ -atic director field from a homogeneously aligned state [1, 57] (Appendix B). We will now exploit this feature to generate and position topological defects through appropriate boundary conditions.

#### B. Defect positioning through boundary anchoring

To illustrate how the total topological charge and the positioning of  $k$ -atic defects can be controlled, we consider numerical solutions of the GL equation (1) on a unit disk domain  $S$  with boundary conditions

$$\Psi_k|_{\partial S} = \exp[i m \gamma_k(\theta)]. \quad (14)$$

Through the prescribed anchoring profile  $\gamma_k(\theta)$ , Eq. (14) fixes the orientation of the  $k$ -atic director along the boundary  $\partial S$  to

$$\phi_{(k)} = \frac{1}{k} \arg(e^{i m \gamma_k}). \quad (15)$$

The examples discussed in the remainder are based on a monotonically increasing profile  $\gamma_k(\theta)$  with  $\gamma_k(2\pi) - \gamma_k(0) = 2\pi$ , for which the boundary condition (14) imposes a total topological charge  $m/k$  in the disk.

The simplest nontrivial anchoring condition (14), corresponding to a topological net charge of  $1/k$  in the disk, is  $m = 1$  and  $\gamma_k = \theta$ . In this case, the GL relaxation dynamics favors the formation of a stationary  $1/k$ -defect at the center of the disk (Fig. 2a; Movie 1). Although this might have been expected on symmetry grounds, it is effectively a consequence of the director field’s bending rigidity mediated by  $L$ : A central position reduces the distortions of the director field around the defect to

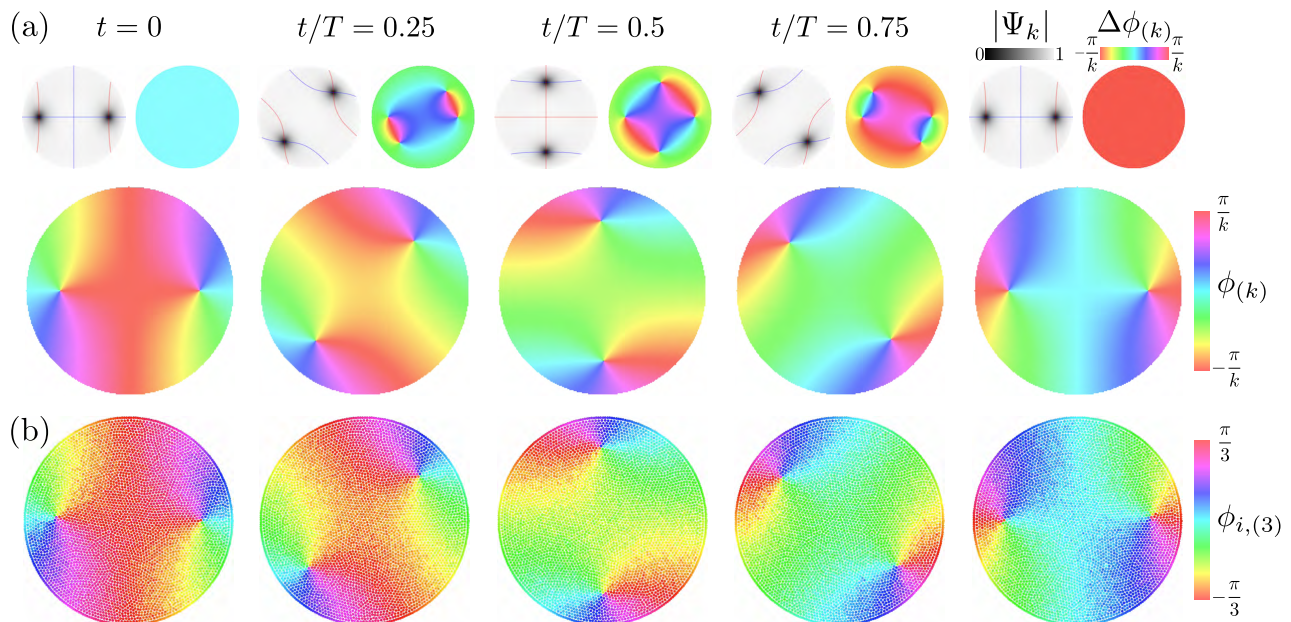


FIG. 3. Demonstration of the anyonic braiding protocol in GL mean-field theory and particle simulations with aligning interactions ( $g > 0$ ) on the unit disk. (a) A pair of symmetric  $1/k$ -defects is braided in GL simulations over the interval  $t/T = [0, 1]$  through a modulation of the boundary anchoring profile as given by Eq. (19). Red and blue lines indicate  $\text{Re}\Psi_k = 0$  and  $\text{Im}\Psi_k = 0$ , respectively. The phase shift defined by  $\Delta\phi_{(k)}(t, r, \theta) := \arg[\exp(ik\delta\phi)]/k$  with  $\delta\phi = \phi_{(k)}(t, r, \theta) - \phi_{(k)}(0, r, \theta)$  assumes the constant global value  $\Delta\phi_{(k)} = \pi/k$  for  $t = T$  (top right; Movie 3). The shown  $k$ -atic phases are exact stationary solutions of the GL, corresponding to perfectly adiabatic braiding with  $T \rightarrow \infty$ . (b) Particle simulations ( $D_r T = 20$ ) for a braided pair of  $1/3$ -defects replicate the GL prediction (Movie 4). The boundary anchoring from Eq. (19) with  $a = 0.1$  was used in both GL and particle simulations, all other parameters are as in Fig. 2d.

a single, monotonous winding that is minimally necessary to be compatible with the boundary conditions.

When imposing  $m = 2$  in Eq. (14), the net topological charge in the disk is  $2/k$ . For suitable initial conditions, this charge may first be concentrated in a single defect, which then splits into a pair of  $1/k$ -defects with lower energy (Fig. 2c; Movie 2). The final steady state reflects that it is energetically favorable to distribute the director field distortions around two  $1/k$  defects, instead of winding the director field symmetrically but with twice the rate around a single  $2/k$  defect. Similarly for  $m > 2$  and  $\gamma_k = \theta$ , transient higher-charge defects decay into  $m$  single  $1/k$ -defects that eventually settle into symmetric low-energy configurations (Fig. S2a,b).

To test if these predictions can indeed be reproduced in the particle model, we simulated Eqs. (6) on a unit disk (Fig. 2b,d), where a particle orientation  $\alpha_i$  corresponds to a  $k$ -atic director orientation

$$\phi_{i,(k)} = \frac{1}{k} \arg(e^{ik\alpha_i}). \quad (16)$$

Comparing this with Eq. (15), the mean-field boundary condition (14) can be matched by fixing the orientations of particles at the boundary to

$$\alpha_i|_{\partial S} = (m/k)\gamma_k. \quad (17)$$

Using the same monotonous boundary-anchoring  $\gamma_k = \theta$ , we find that the resulting particle simulations agree well

with the GL theory (Fig. 2b,d and Fig. S2a,b). For example, for  $k = 3$  and  $m = 1$ , a single  $1/3$ -defect forms and moves to the center of the domain (Fig. 2b; Movie 1), whereas for  $k = 3$  and  $m = 2$ , an initially created  $2/3$ -defect splits into two  $1/3$ -defects that move symmetrically away from each other until they reach a symmetric steady state position (Fig. 2d; Movie 2). In both cases, the final steady state textures confirm the GL mean-field prediction.

The above examples illustrate how topological defects take equilibrium positions that effectively minimize director winding gradients around them. It follows that for a constant azimuthal anchor-winding gradient ( $\partial_\theta \gamma_k = \text{const.}$ ) at the disk boundary, the equilibrium positions of defect-pairs are degenerate with respect to rotations around the disk center. In turn, structured anchoring enables a targeted defect positioning. We demonstrate this useful fact by controlling the orientation of the axis connecting a  $1/k$ -defect pair. To this end, we consider Eq. (14) with  $m = 2$  and

$$\gamma_k(\theta) = \theta + a \sin[2(\theta - \theta_0)], \quad (18)$$

where  $|a| < 1/2$  ensures that  $\gamma_k(\theta)$  is monotonic. The choice of this anchoring profile is motivated as follows: For  $\theta_0 = 0$  and  $a > 0$ , the azimuthal anchor-winding gradient  $\partial_\theta \gamma$  becomes maximal at  $\theta = 0, \pi$  and minimal at  $\theta = \pi/2, 3\pi/2$ . It is therefore energetically favorable

for topological defects to be closer to the boundary at  $\theta = 0, \pi$  than at  $\theta = \pi/2, 3\pi/2$ . Consequently, the axis of a defect pair aligns with the  $x$ -axis in this case (Fig. 3a). An analogous reasoning for arbitrary  $\theta_0$  implies that the boundary condition (18) orients defect pairs along the axis  $(\cos \theta_0, \sin \theta_0)$  when  $a > 0$ . In the next part, we will use a dynamic generalization of the anchoring profile Eq. (18) to realize defect braiding protocols in both continuum and particle simulations.

### C. Braiding through adiabatic boundary modulation

We now demonstrate how one can implement an anyonic braiding protocol [31, 37] by adiabatically changing the anchoring profile (18). Specifically, we aim to braid an identical defect pair such that the phase of the final state  $\Psi_k(t = T)$  differs from that of the initial state  $\Psi_k(t = 0)$  by a constant global shift  $\Delta\phi$ , which means that  $\Psi_k(T, r, \theta) = e^{i\Delta\phi}\Psi_k(0, r, \theta)$ . To this end, we consider a pair of  $1/k$ -defects that is initially aligned with the  $x$ -axis (Fig. 3a,  $t = 0$ ). As discussed above, this configuration can be achieved by imposing the anchoring condition (14) with  $m = 2$  and  $\theta_0 = 0$  in Eq. (18). To parameterize the braiding operation, we write Eq. (18) in the more general form  $\gamma_k(\theta, t) = \theta_1 + a \sin 2\theta_2$  and consider a continuously changing anchoring profile with

$$\theta_1(\theta, t) = \theta - \frac{\pi t}{2T}, \quad \theta_2(\theta, t) = \theta - \frac{\pi t}{T} \quad (19)$$

for  $t \in [0, T]$ . In the adiabatic limit  $T \rightarrow \infty$ , this protocol parameterizes a unique sequence of stationary states. In Eq. (19), the parametric changes of  $\theta_1$  and  $\theta_2$  implement a rotation of the  $k$ -atic director anchoring by  $\pi/k$  and a rotation of the preferred localization axis of the defect pair by  $\pi$ , respectively. In both GL equation (Fig. 3a; Movie 3) and microscopic particle model (Fig. 3b; Movie 4), this protocol exchanges the two identical defects and transforms the initial state  $\Psi_k(0, r, \theta)$  into a final state  $\Psi_k(T, r, \theta) = e^{i\pi/k}\Psi_k(0, r, \theta)$ , with the stochastic particle model progressing through a noisy realization of the texture sequence predicted by the GL mean-field theory.

More generally, this demonstration shows how one can implement a classical analog of an anyonic exchange symmetry in the complex order-parameter field of DLCs. We emphasize, however, that a global phase change in the  $k$ -atic director field necessitates a corresponding phase change at the boundary.

## V. SPONTANEOUS CHIRAL SYMMETRY BREAKING AND BRAIDING IN ANTI-ALIGNING DLCs ( $g < 0$ )

Having focused on aligning interactions in the previous section, we now consider  $k$ -atic DLCs with short-range anti-aligning interactions ( $g < 0$ ; Fig. 1a,b). In this

case, the mean-field model in Eq. (1) takes the form of a Swift-Hohenberg (SH) equation for the complex order parameter  $\Psi_k$ . When the boundary anchoring imposes a topological charge of  $1/k$  on a unit disk, we find that the SH equation predicts a spontaneous chiral symmetry breaking of texture patterns that is also observed in the microscopic model. Last but not least, to demonstrate the versatility of the braiding protocol from Sec. IV C, we will perform an anyonic braiding operation for a defect pair in anti-aligning DLCs in both SH equation and microscopic model.

### A. SH mean-field theory for anti-aligning $k$ -atics

We consider the microscopic model Eq. (6) with  $g < 0$ , which favors anti-aligning configurations of nearby  $k$ -atic particle directors. For a small but finite interaction range  $R_\alpha > 0$ , the mean-field dynamics of the  $k$ -atic mode can be approximated by (Appendix A)

$$\bar{\tau} \partial_t \psi_k \approx F_k^{(0)} - (\beta_1 R_\alpha^2 \nabla^2 + \beta_2 R_\alpha^4 \nabla^2 \nabla^2) \psi_k, \quad (20)$$

where the homogeneous terms  $F_k^{(0)}$  were defined previously in Eq. (10). The coefficients  $\beta_1$  and  $\beta_2$  in Eq. (20) depend on the spatial interaction kernel of the microscopic model. Assuming, as before, equally weighted interactions between particles within a neighborhood of radius  $R_\alpha$ , the kernel determines the dispersion relation for perturbations of the  $k$ -atic mode  $\psi_k \sim f_k$  around the disordered state  $f_k = 0$ , which is approximated by the parameters  $\beta_1$  and  $\beta_2$  (Appendix A 2).

The coarse-graining result Eq. (20) implies a mean-field model for anti-aligning DLCs of the general form Eq. (1) with

$$\mathcal{L}(\nabla^2) = -L_1^2 \nabla^2 - L_2^4 \nabla^2 \nabla^2, \quad (21)$$

corresponding to a SH equation [46] for the complex order parameter  $\Psi_k$ . Equation (20) specifies the mean-field parameters  $L_1$  and  $L_2$  in Eq. (21) in terms of the interaction radius  $R_\alpha$  as

$$L_1 \simeq \beta_1^{1/2} R_\alpha \quad L_2 \simeq \beta_2^{1/4} R_\alpha. \quad (22)$$

The ratio  $L_2^2/L_1$  signals an emergent mesoscopic length-scale in the phase field, arising from the competition between anti-aligning particle interactions.

### B. Spontaneous chiral symmetry breaking of texture patterns

Even when microscopic particles are reflection invariant, the interplay between anti-aligning particle interactions and boundary conditions can give rise to an interesting spontaneous chiral symmetry breaking phenomenon. To demonstrate this, we compare the nonlinear dynamics of 3-fold symmetric particles described by

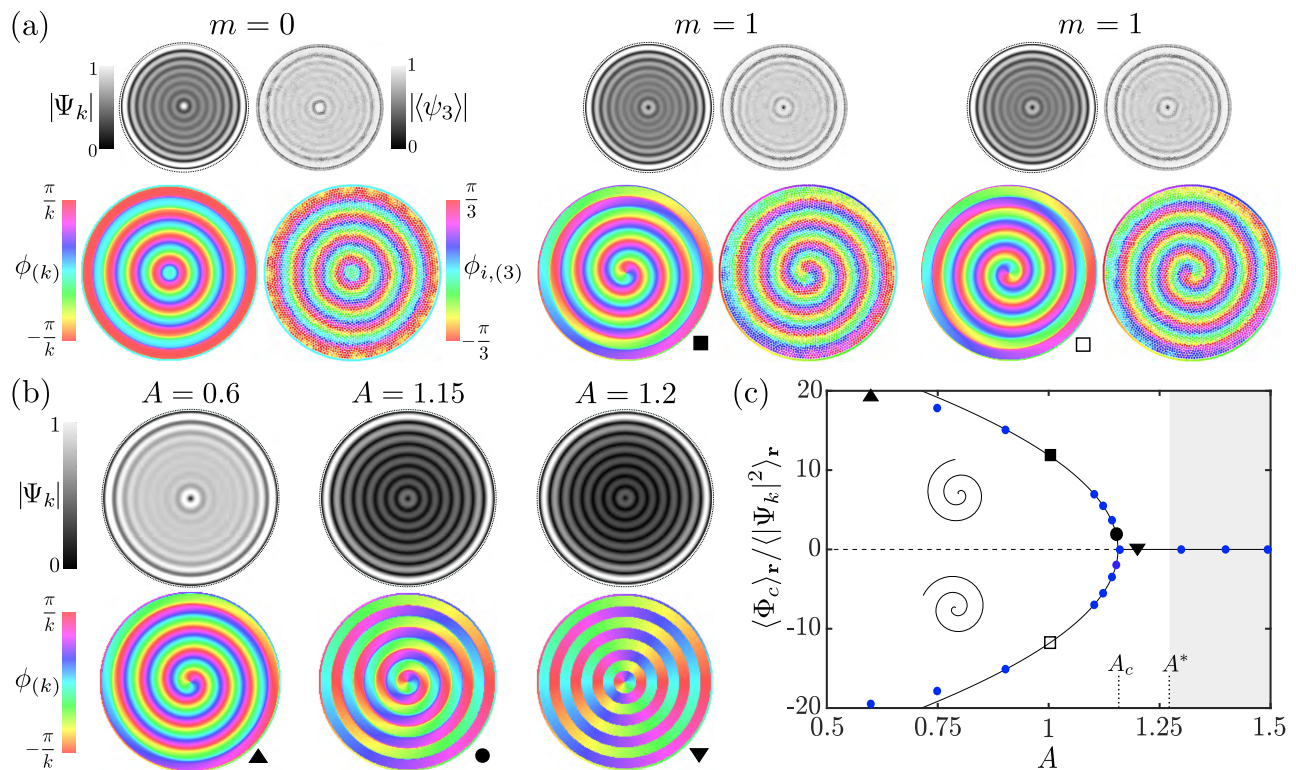


FIG. 4. Chiral symmetry breaking in phase field textures of the SH mean-field theory and particle simulations with anti-aligning interactions ( $g < 0$ ) on a unit disk. (a) Stationary order-parameters (top) and phase-field solutions (bottom) for the mean-field Eq. (1) with  $\mathcal{L} = -L_1^2 \nabla^2 - L_2^4 (\nabla^2)^2$  and particle model Eq. (6) with anti-aligning interactions, using the boundary anchoring from Eq. (14) with  $\gamma_k = \theta$ . A stationary defect-free axisymmetric state exists for topologically trivial boundary anchoring with  $m = 0$ . For  $m = 1$ , chiral textures with  $1/k$ -defect at the center form spontaneously in both mean-field and particle simulations (Movie 5). Mean-field simulation parameters were  $A = B = 1$ ,  $L_1$  and  $L_2$  as defined in Eq. (22) with  $\beta_1 = 0.1$ ,  $\beta_2 = 0.002$  and  $R_\alpha = 0.2$ . Particle simulation parameters:  $k = 3$ ,  $g = -1$ , and all other parameters as in Fig. 2d. (b) Examples of spontaneously formed stationary solution of the SH model for  $m = 1$  and selected values of the control parameter  $A$  with parameters identical to those in panel (a). (c) The phase-chirality parameter  $\Phi_c$  defined in Eq. (23) characterizes the spontaneous symmetry-breaking into chiral textures of different handedness ( $\langle \cdot \rangle_r$  denotes a spatial averages). The bulk dynamics of the SH model is linearly stable for  $A > A^*$  (gray-shaded region), but achiral ring patterns remain due to the boundary anchoring Eq. (14) with  $|\Psi_k|_{\partial S} = 1$ . Phase phase-chirality parameters measured in additional simulations for different values of  $A$  (small blue dots) approach the curve  $\sim \pm \sqrt{A_c - A}$  for  $A \searrow A_c$  with  $A_c \approx 1.155$ , consistent with a supercritical pitchfork bifurcation.

$k = 3$  and  $g < 0$  in Eq. (6) with predictions from the corresponding SH mean-field Eq. (1). As before, we assume that particles are confined to a unit disc.

We first consider a topologically trivial boundary anchoring corresponding to  $m = 0$  in Eq. (14). In this case, the SH mean-field theory predicts the existence of defect-free azimuthally symmetric stationary states that can indeed be observed in simulations of the anti-aligning particle model (Fig. 4a, left). However, although such defect-free states are long-lived in the presence of noise, they only form from suitably pre-patterned initial conditions (Appendix D), whereas random initial conditions typically lead to ring-shaped patterns that are intersected by chains of  $\pm 1/k$ -point defects with zero topological net charge (Fig. S2c).

For a boundary anchoring Eq. (14) with  $\gamma_k = \theta$  and  $m = 1$ , the SH mean-field theory predicts the sponta-

neous formation of a spiral-shaped chiral texture with a  $1/k$ -defect at the center of the disk, while the  $k$ -atic order parameter  $|\Psi_k|$  maintains an azimuthal symmetry. Again, the particle model confirms this prediction (Fig. 4a, right and Movie 5). Such chiral textures are reminiscent of spiral patterns that have recently been observed theoretically and experimentally in cholesteric LCs [58, 59]. However, the latter arise from chiral microscopic interactions, while spiral texture patterns in our system arise from a spontaneous symmetry breaking among isotropically interacting achiral particles.

Upon varying  $A$  in simulations of the SH Eq. (1), while keeping all other parameters fixed, we find that textures become chiral only below a critical value  $A_c$  but remain azimuthally symmetric if  $A > A_c$  (Fig. 4b,c). To quantify this transition, we introduce the phase-chirality param-

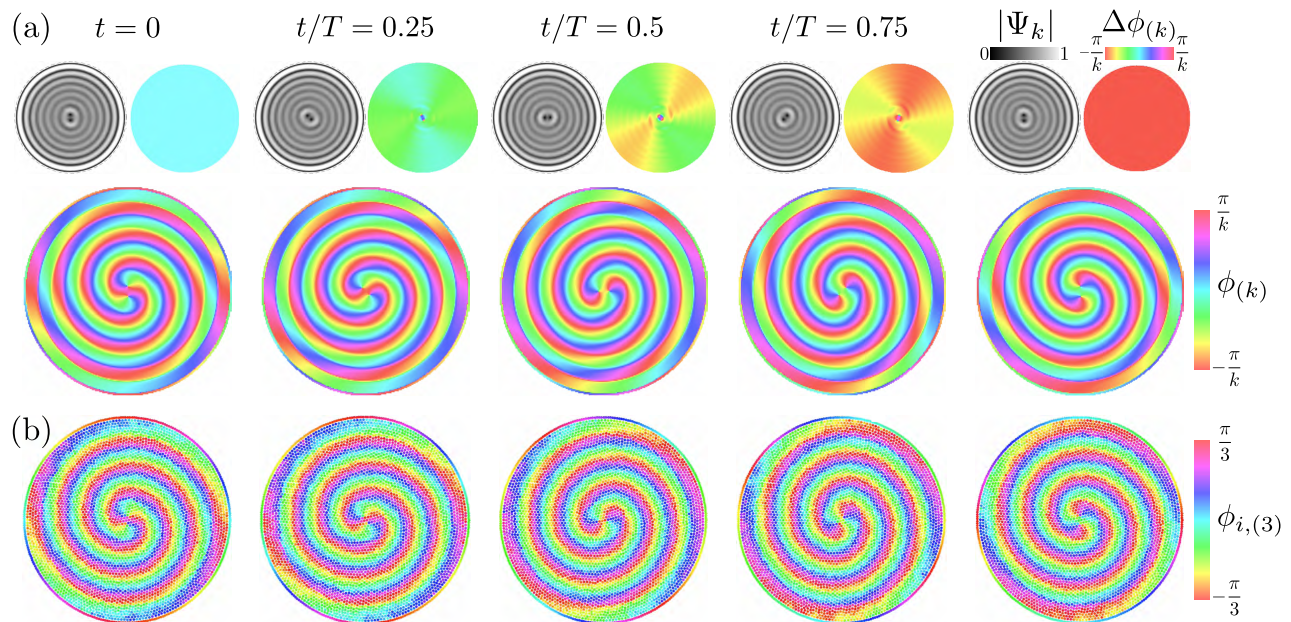


FIG. 5. Demonstration of the anyonic braiding protocol in (a) the SH mean-field theory and (b) particle simulations with anti-alignment interactions ( $g < 0$ ) on the unit disk (Movies 6 and 7). A boundary anchoring with  $m = 2$  imposes a total defect charge of  $2/k$  on the domain, supporting two stable  $1/k$  point defects near the disc center and outwards spiraling textures. Similar to Fig. 3, we applied the boundary-controlled braiding protocol from Eq. (19) with  $a = 0.2$ , while using the model parameters from Fig. 4. The  $k$ -atic mean-field phase fields in (a) are exact stationary solutions of the SH Eq. (1), corresponding to perfectly adiabatic braiding with  $T \rightarrow \infty$ . In both mean-field and particle simulations, the initial defect-pair state does not form spontaneously from random initial conditions, but can be robustly generated as a stationary state from initial conditions that are sufficiently close to a double-spiral texture (Appendix D). The braiding protocol is started at  $t = 0$  by modulating the boundary anchoring as described in Sec. IV C. At the end of the braiding process, the two point defects have exchanged their position and the director field has acquired a constant global phase shift  $\Delta\phi_{(k)}$  of  $\pi/k$  in the  $k$ -atic SH equation (a) and of  $\pi/3$  in the 3-atic anti-aligning particle model (b).

ter (Appendix C)

$$\Phi_c = k|\Psi_k|^2 \mathbf{e}_r \cdot \nabla \phi_{(k)}. \quad (23)$$

This quantity characterizes chiral signatures in textures around a defect by measuring the radial contributions in the  $k$ -atic phase gradient. In particular,  $\Phi_c > 0$  ( $\Phi_c < 0$ ) indicates in our system the presence of right-handed (left-handed) texture spirals leading into the defect (Fig. 4c). Averaging  $\Phi_c$  across the disc domain, we observe a continuous transition from achiral to chiral textures at  $A_c$ . The transition exhibits the characteristics of a supercritical pitchfork bifurcation with left- and right-handed texture patterns forming with equal probability depending on the initial conditions (Fig. 4c). We note that the transition point  $A_c$  differs from the linear stability threshold  $A^*$  of the SH equation. While at  $A^*$  some Fourier mode becomes unstable for the first time, several modes need to be unstable for chiral patterns to emerge, requiring that  $A < A_c < A^*$  (Fig. 4c).

### C. Braiding of chiral texture patterns

Similar to their achiral counterparts, chiral defect pairs in anti-aligning DLCs can also be braided by applying

the adiabatic protocol from Sec. IV C. To demonstrate this, we use in both SH mean-field and particle simulations the boundary condition Eq. (14) with  $m = 2$  and fix the anchoring profile  $\gamma_k$  from Eq. (18) with  $a = 0.2$ . This boundary condition stabilizes now a vertically oriented pair of  $1/k$  defects near the disk center, which is surrounded by texture spirals that intertwine towards the boundary (Fig. 5,  $t = 0$ ). To prepare this initial state in the continuum and particle simulations, one can let the system relax from suitably pre-patterned textures (Appendix D). The resulting two-defect state is stable and can be robustly braided using the anchoring profile parameterization given in Eq. (19). Snapshots of the braiding sequences, selected from Movies 6 and 7, are shown in Fig. 5. At the end of the braiding operation, the defects have exchanged their positions and the complex order parameter field  $\Psi_k$  has acquired a constant global phase shift  $\Delta\phi_{(k)} = \pi/k$ , reminiscent of anyonic particle exchange in quantum systems.

## VI. CONCLUSIONS

The above analysis shows that the relaxation behavior and adiabatic manipulation of 2D liquid crystals com-

posed of  $k$ -fold symmetric particles can be accurately described within a unified mean-field theory for a complex order-parameter field. Due to the generic character of the underlying particle model, which merely assumed overdamped short-range  $XY$ -type interactions on a disordered lattice, we expect that the above ideas can be experimentally implemented and tested in different ways. Promising candidates include colloidal systems [3, 4] with predefined symmetries and controllable steric [9, 11, 13], magnetic [43, 60] or chemical [8, 61] interactions. The main experimental challenge will be to enforce the required short-range orientational interactions while simultaneously suppressing positional order. This could, for example, be achieved by ‘gluing’ mutually repulsive  $k$ -atic elements, as realized in Fig. 1d via magnetic dipole interactions, onto multi-disperse disks with a suitably chosen radius distribution. Other promising candidate systems could be thin films of 3-fold symmetric

molecules, such as 1,3,5-trichlorobenzene [19], or  $k$ -fold symmetric DNA-origami structures [40, 41], building on recently developed experimental techniques [42] for the assembly and control of DNA-origami-based liquid crystals.

From a general theoretical perspective,  $k$ -atic DLC systems [28] provide a useful classical framework for studying and visualizing fractional topological excitations and their exchange properties. Since the energetic correspondence with quantum fluids only holds at the mean-field level, it remains an interesting open question whether and how the statistical properties of fractional defects in DLCs depend on their braiding behavior. In addition, the above results suggest multiple directions for future research, including generalizations to passive and active [62]  $k$ -atic hydrodynamic systems in two and three dimensions, which can be expected to exhibit new forms of energy transport and turbulence [16, 63].

---

\* amietke@mit.edu

† dunkel@mit.edu

- [1] P. G. de Gennes and J. Prost, *The Physics of Liquid Crystals* (Clarendon Press, 1993).
- [2] P. M. Chaikin and T. C. Lubensky, *Principles of Condensed Matter Physics* (Cambridge University Press, 2000).
- [3] Q. Liu, P. J. Ackerman, T. C. Lubensky, and I. I. Smalyukh, Proc. Natl. Acad. Sci. U.S.A. **113**, 10479 (2016).
- [4] M. Niederberger, Adv. Funct. Mater. **27**, 1703647 (2017).
- [5] M. Fruchart, Y. Zhou, and V. Vitelli, Nature **577**, 636 (2020).
- [6] Z. L. Wang and X. Feng, J. Phys. Chem. B **107**, 13563 (2003).
- [7] H. Dong, S.-R. Du, X.-Y. Zheng, G.-M. Lyu, L.-D. Sun, L.-D. Li, P.-Z. Zhang, C. Zhang, and C.-H. Yan, Chem. Rev. **115**, 10725 (2015).
- [8] G.-R. Yi, D. J. Pine, and S. Sacanna, J. Phys. Condens. Matter **25**, 193101 (2013).
- [9] H. R. Vutukuri, A. Imhof, and A. van Blaaderen, Angew. Chem. Int. Ed. **53**, 13830 (2014).
- [10] M. Sindoro, N. Yanai, A.-Y. Jee, and S. Granick, Acc. Chem. Res. **47**, 459 (2014).
- [11] B. Li, D. Zhou, and Y. Han, Nature Rev. Mater. **1**, 1 (2016).
- [12] C. Avci, I. Imaz, A. Carné-Sánchez, J. A. Pariente, N. Tasios, J. Pérez-Carvajal, M. I. Alonso, A. Blanco, M. Dijkstra, C. López, and D. MasPOCH, Nat. Chem. **10**, 78 (2018).
- [13] Y. Wang, Y. Wang, X. Zheng, G.-R. Yi, S. Sacanna, D. J. Pine, and M. Weck, J. Am. Chem. Soc. **136**, 6866 (2014).
- [14] A.-C. Genix and J. Oberdisse, Soft Matter **14**, 5161 (2018).
- [15] K. Zhao and T. G. Mason, Rep. Prog. Phys. **81**, 126601 (2018).
- [16] L. Giomi, Phys. Rev. X **5**, 031003 (2015).
- [17] S. Dussi and M. Dijkstra, Nat. Comm. **7**, 11175 (2016).
- [18] J. A. Anderson, J. Antonaglia, J. A. Millan, M. Engel, and S. C. Glotzer, Phys. Rev. X **7**, 021001 (2017).
- [19] M. J. Bowick, O. V. Manyuhina, and F. Serafin, EPL **117**, 26001 (2017).
- [20] A. J. Beekman, J. Nissinen, K. Wu, K. Liu, R.-J. Slager, Z. Nussinov, V. Cvetkovic, and J. Zaanen, Phys. Rep. **683**, 1 (2017).
- [21] P. Sartori and C. F. Lee, New J. Phys. **21**, 073064 (2019).
- [22] A. Maitra, M. Lenz, and R. Voituriez, Phys. Rev. Lett. **125**, 238005 (2020).
- [23] P. G. de Gennes, Solid State Comm. **10**, 753 (1972).
- [24] B. I. Halperin and T. C. Lubensky, Solid State Commun. **14**, 997 (1974).
- [25] B. I. Halperin, T. C. Lubensky, and S. Ma, Phys. Rev. Lett. **32**, 292 (1974).
- [26] Pershan, P.S. and Prost, J., J. Phys. Lett. **40**, 27 (1979).
- [27] S. R. Renn and T. C. Lubensky, Phys. Rev. A **38**, 2132 (1988).
- [28] M. J. Bowick and L. Giomi, Adv. Phys. **58**, 449 (2009).
- [29] B. Zappone, A. E. Mamuk, I. Gryn, V. Arima, A. Zizzari, R. Bartolino, E. Lacaze, and R. Petschek, Proc. Natl. Acad. Sci. U. S. A. **117**, 17643 (2020).
- [30] F. Wilczek, Phys. Rev. Lett. **49**, 957 (1982).
- [31] S. R. Lee, P. A. Sharma, A. L. Lima-Sharma, W. Pan, and T. M. Nenoff, Chem. Mater. **31**, 26 (2019).
- [32] J. M. Leinaas and J. Myrheim, Il Nuovo Cimento B **37**, 1 (1977).
- [33] R. B. Laughlin, Phys. Rev. Lett. **50**, 1395 (1983).
- [34] D. Arovas, J. R. Schrieffer, and F. Wilczek, Phys. Rev. Lett. **53**, 722 (1984).
- [35] B. I. Halperin, Scientific American **254**, 52 (1986).
- [36] A. Kitaev, Ann. Physics **303**, 2 (2003).
- [37] C. Nayak, S. H. Simon, A. Stern, M. Freedman, and S. Das Sarma, Rev. Mod. Phys. **80**, 1083 (2008).
- [38] J. Nakamura, S. Fallahi, H. Sahasrabudhe, R. Rahman, S. Liang, G. C. Gardner, and M. J. Manfra, Nat. Phys. **15**, 563 (2019).
- [39] H. Bartolomei, M. Kumar, R. Bisognin, A. Marguerite, J.-M. Berroir, E. Bocquillon, B. Plaças, A. Cavanna, Q. Dong, U. Gennser, Y. Jin, and G. Fève, Science **368**, 173 (2020).
- [40] J. Chao, H. Zhang, Y. Xing, Q. Li, H. Liu, L. Wang,

- L. Wang, and C. Fan, *Nat. Protoc.* **13**, 1569 (2018).
- [41] R. Veneziano, S. Ratanalert, K. Zhang, F. Zhang, H. Yan, W. Chiu, and M. Bathe, *Science* **352**, 1534 (2016).
- [42] M. Siavashpouri, C. H. Wachauf, M. J. Zakhary, F. Praetorius, H. Dietz, and Z. Dogic, *Nat. Mater.* **16**, 849 (2017).
- [43] V. Soni, E. S. Bililign, S. Magkiriadou, S. Sacanna, D. Bartolo, M. J. Shelley, and W. T. M. Irvine, *Nat. Phys.* **15**, 1188 (2019).
- [44] E. W. Gehrels, W. B. Rogers, and V. N. Manoharan, *Soft Matter* **14**, 969 (2018).
- [45] I. S. Aranson and L. Kramer, *Rev. Mod. Phys.* **74**, 99 (2002).
- [46] M. Cross and H. Greenside, *Pattern Formation and Dynamics in Nonequilibrium Systems* (Cambridge University Press, 2009).
- [47] E. P. Gross, *Il Nuovo Cimento* **20**, 454 (1961).
- [48] V. Heinonen, K. J. Burns, and J. Dunkel, *Phys. Rev. A* **99**, 063621 (2019).
- [49] J. M. Kosterlitz and D. J. Thouless, *J. Phys. Condens. Matter* **6**, 1181 (1973).
- [50] J. McCarthy, *Nucl. Phys. B* **275**, 421 (1986).
- [51] D. S. Dean, *J. Phys. A* **29**, L613 (1996).
- [52] E. Bertin, M. Droz, and G. Grégoire, *J. Phys. A* **42**, 445001 (2009).
- [53] F. D. C. Farrell, M. C. Marchetti, D. Marenduzzo, and J. Tailleur, *Phys. Rev. Lett.* **108**, 248101 (2012).
- [54] R. Großmann, P. Romanczuk, M. Bär, and L. Schimansky-Geier, *Phys. Rev. Lett.* **113**, 258104 (2014).
- [55] K. H. Nagai, Y. Sumino, R. Montagne, I. S. Aranson, and H. Chaté, *Phys. Rev. Lett.* **114**, 168001 (2015).
- [56] D. Arold and M. Schmiedeberg, *J. Phys. Condens. Matter* **32**, 315403 (2020).
- [57] S. Chandrasekhar, *Liquid Crystals* (Cambridge University Press, 1992).
- [58] J. Pollard, G. Posnjak, S. Čopar, I. Mušević, and G. P. Alexander, *Phys. Rev. X* **9**, 021004 (2019).
- [59] L. Tran and K. J. M. Bishop, *ACS Nano* **14**, 5459 (2020).
- [60] B. A. Grzybowski, H. A. Stone, and G. M. Whitesides, *Nature* **405**, 1033 (2000).
- [61] A. Walther and A. H. E. Müller, *Chem. Rev.* **113**, 5194 (2013).
- [62] H. H. Wensink, H. Löwen, M. Marechal, A. Härtel, R. Wittkowski, U. Zimmermann, A. Kaiser, and A. M. Menzel, *Eur. Phys. J. ST* **222**, 3023 (2013).
- [63] R. Alert, J.-F. Joanny, and J. Casademunt, *Nat. Phys.* **16**, 682 (2020).
- [64] E. Bertin, A. Baskaran, H. Chaté, and M. C. Marchetti, *Phys. Rev. E* **92**, 042141 (2015).
- [65] B. Liebchen, M. E. Cates, and D. Marenduzzo, *Soft Matter* **12**, 7259 (2016).
- [66] A. U. Oza and J. Dunkel, *New J. Phys.* **18**, 093006 (2016).
- [67] E. Bodenschatz, W. Pesch, and L. Kramer, *Physica D* **32**, 135 (1988).
- [68] “Matlab 2019b,” The MathWorks, Natick, MA, USA.
- [69] K. J. Burns, G. M. Vasil, J. S. Oishi, D. Lecoanet, and B. P. Brown, *Phys. Rev. Research* **2**, 023068 (2020).
- [70] P. E. Kloeden and E. Platen, *Numerical Solution of Stochastic Differential Equations* (Springer Berlin Heidelberg, 2011).

## APPENDIX

## Appendix A: Coarse-graining of the microscopic model

We describe the coarse-graining of the minimal microscopic model Eq. (6) and show how spatial interactions with finite-range range  $R_\alpha$  give rise to the operators  $\mathcal{L} = R_\alpha^2 \nabla^2 / 8$  and  $\mathcal{L} = -\beta_1 R_\alpha^2 \nabla^2 - \beta_2 R_\alpha^4 (\nabla^2)^2$  in the

$$\partial_t f(\mathbf{r}, \alpha, t) = \frac{g}{\pi R_\alpha^2} \partial_\alpha \iint f(\mathbf{r}, \alpha, t) f(\mathbf{r}', \alpha', t) \sin[k(\alpha - \alpha')] \hat{I}(\mathbf{r} - \mathbf{r}') d\alpha' d\mathbf{r}' + D_r \partial_\alpha^2 f. \quad (\text{A1})$$

It is convenient to define an effective, normalized interaction kernel as  $I(\mathbf{r}) = \hat{I}(\mathbf{r}) / (\pi R_\alpha^2)$ . Using the Fourier-representations

$$f(\mathbf{r}, \alpha, t) = \frac{1}{(2\pi)^3} \sum_{n \in \mathbb{Z}} \int d\mathbf{q} \tilde{f}_n(\mathbf{q}, t) e^{-i(n\alpha + \mathbf{r} \cdot \mathbf{q})} \quad (\text{A2})$$

$$I(\mathbf{r}) = \frac{1}{(2\pi)^2} \int d\mathbf{q} \tilde{I}(\mathbf{q}) e^{-i\mathbf{r} \cdot \mathbf{q}} \quad (\text{A3})$$

$$\partial_t f_n(\mathbf{r}, t) = \frac{gn}{8\pi^2} \int \left[ f_{n-k}(\mathbf{r}, t) \tilde{f}_k(\mathbf{q}, t) - f_{n+k}(\mathbf{r}, t) \tilde{f}_{-k}(\mathbf{q}, t) \right] \tilde{I}(\mathbf{q}) e^{-i\mathbf{r} \cdot \mathbf{q}} d\mathbf{q} - D_r n^2 f_n(\mathbf{r}, t), \quad (\text{A5})$$

where, for convenience, we chose a mixed representation in terms of  $f_n(\mathbf{r}, t)$  and  $\tilde{f}_k(\mathbf{q}, t)$ .

## a. Point-wise interactions

We first discuss the limit of point-wise interactions, corresponding to  $I(\mathbf{r}) = \delta(\mathbf{r})$  and  $\tilde{I} = 1$ , which has been widely used in models that contain polar ( $k = 1$ ) and nematic ( $k = 2$ ) alignment interactions [52, 64, 65] as given in Eq. (6). In this case, Eqs. (A5) simplify to a spatially homogeneous system of equations

$$\partial_t f_n = \frac{gn}{2} (f_{n-k} f_k - f_{n+k} f_{-k}) - D_r n^2 f_n. \quad (\text{A6})$$

This system can be further split into a subset of coupled equations for the modes  $n = jk$  with integers  $j \neq 0$ :

$$\partial_t f_{jk} = \frac{gjk}{2} (f_{(j-1)k} f_k - f_{(j+1)k} f_{-k}) - D_r (jk)^2 f_{jk} \quad (\text{A7})$$

coarse-grained dynamics Eqs. (12) and (20), respectively.

## 1. Hierarchy of mode equations and linearization

We follow the standard coarse-graining approach [51–53], by using Itô calculus, neglecting multiplicative noise terms and factorizing pair correlations, to derive a dynamic equation for the one-particle probability density function  $f(\alpha, \mathbf{r}, t)$  from the microscopic model Eq. (6). For a general interaction kernel  $\hat{I}(\mathbf{r})$  that describes how the orientational interactions with neighboring particles are spatially weighted, this equation takes the form

in Eq. (A1), we can find a hierarchy of coupled dynamic equations for the modes

$$f_n(\mathbf{r}, t) = \frac{1}{(2\pi)^2} \int d\mathbf{q} \tilde{f}_n(\mathbf{q}, t) e^{-i\mathbf{r} \cdot \mathbf{q}}. \quad (\text{A4})$$

For  $k$ -atic interactions as given in the microscopic model Eq. (6), this hierarchy takes the form

and a system of equations for the modes  $f_n$  with  $n \neq jk$ , where the latter modes always vanish at long times. We then generalize the standard closure assumption of a fast relaxation of the next coupled mode [52] to the case of a  $k$ -atic system, which corresponds to assuming  $\partial_t f_{2k} = 0$  and  $f_{sk} = 0$  for integers  $s \geq 3$ . From Eqs. (A7), we find in this case a steady-state value for  $f_{2k}$  and consequently the closed coarse-grained dynamics

$$\partial_t f_k = \frac{g\rho k}{2} \left( 1 - \frac{2D_r k}{g\rho} \right) f_k - \frac{g^2}{8D_r} |f_k|^2 f_k. \quad (\text{A8})$$

Using the dimensionless  $k$ -atic mode  $\psi_k = f_k / \rho$  in Eq. (A8), we arrive at the final coarse-graining result given in Eq. (10).

b.  $k$ -atic order parameter in particle simulations

To approximate the normalized  $k$ -atic mode  $\psi_k = f_k / \rho$  in particle simulations, we use the classical  $k$ -atic order

parameter [2]

$$\psi_k(\mathbf{r}_i) = \frac{1}{|\mathcal{N}_i|} \sum_{j \in \mathcal{N}_i} e^{ik\alpha_j}, \quad (\text{A9})$$

where the sum is evaluated with respect to all particles  $j$  within a neighbourhood  $\mathcal{N}_i$  of particle  $i$ . This can be motivated as follows: Using Eqs. (7) and (8), and ignoring time for brevity, we have

$$\begin{aligned} f_k(\mathbf{r}_i) &= \int_0^{2\pi} d\alpha \sum_j \langle \delta(\mathbf{r}_i - \mathbf{r}_j) \delta(\alpha - \alpha_j) \rangle e^{ik\alpha} \\ &\approx \frac{1}{\pi R_i^2} \left\langle \int_0^{2\pi} d\alpha \sum_{j \in \mathcal{N}_i} \delta(\alpha - \alpha_j) e^{ik\alpha} \right\rangle \\ &\approx \rho \langle \psi_k(\mathbf{r}_i) \rangle. \end{aligned} \quad (\text{A10})$$

Here,  $R_i$  denotes the neighborhood radius and in the last step we have used that particles are homogeneously distributed, such that  $|\mathcal{N}_i|/(\pi R_i^2) \approx \rho$ . To compute the order parameter  $\langle \psi_k(\mathbf{r}_i) \rangle$  for stationary states, we have replaced the Gaussian white-noise average by temporal averages.

### c. Linearization with an arbitrary interaction kernel

For fixed, homogeneous particle number density  $\rho = f_0$  the mode coupling terms under the integral in the system of Eqs. (A5) only contain a linear contribution when  $|n| = k$ . As a result, the full linearization of Eq. (A5) around  $f_n = 0$  is for  $|n| \neq k$  simply given by

$$\partial_t f_n = -D_r n^2 f_n, \quad (\text{A11})$$

and reads for  $|n| = k$ :

$$\partial_t \tilde{f}_k(\mathbf{q}, t) = \frac{g\rho k}{2} \left[ \tilde{I}(\mathbf{q}) - \frac{2D_r k}{g\rho} \right] \tilde{f}_k(\mathbf{q}, t). \quad (\text{A12})$$

Equation (A12) defines the dispersion relation for the  $k$ -atic mode dynamics near the disordered state and holds for arbitrary spatial interaction kernels.

## 2. Approximation of the pseudo-differential operator and dispersion relation

In the microscopic model Eq. (6), we consider an isotropic interaction neighborhood, such that the interaction kernel in Fourier-space must be an even function that depends only on the wave vector amplitude  $q = |\mathbf{q}|$ . Assuming that  $\tilde{I}(x)$  can be expanded in a suitable power-series

$$\tilde{I}(x) = 1 + \sum_{j=1}^{\infty} \beta_j x^{2j}, \quad (\text{A13})$$

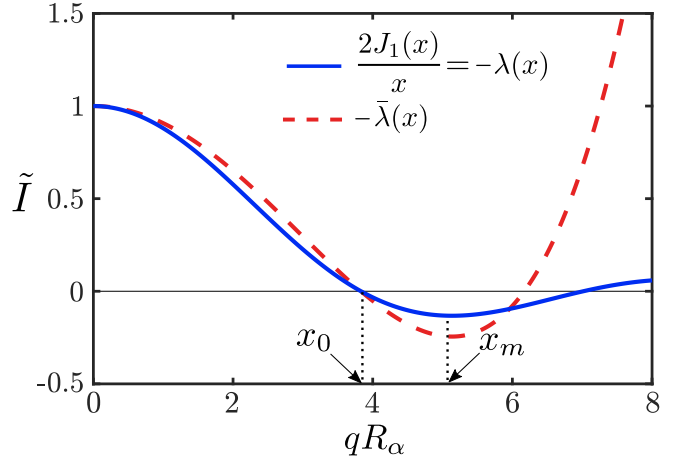


FIG. S1. Fourier-space representation of the interaction kernel  $\tilde{I}(x) = -2J_1(x)/x$  (solid line) used in the microscopic particle model Eq. (6), where  $J_1$  denotes the Bessel function of the first kind. The linearized mode dynamics Eq. (A12) implies for  $D_r/(|g|\rho) \ll 1$  that  $\lambda = -\tilde{I}(q)$  essentially represents the dispersion relation of the  $k$ -atic particle model with anti-aligning interactions ( $g < 0$ ). An empirical approximation  $-\tilde{\lambda} = 1 - \beta_1 x^2 + \beta_2 x^4$  (dashed line) is then chosen such that the smallest unstable wavelength set by the first root  $x_0$  and the most unstable wavelength set by  $x_m$  are the same for  $\tilde{\lambda}$  and  $\lambda$ . This yields Eq. (20) with  $\beta_1 \approx 0.1$  and  $\beta_2 \approx 0.002$ .

Eq. (A12) has an equivalent interpretation in real space that is given by

$$\partial_t f_k(\mathbf{r}, t) = \frac{g\rho k}{2} \left[ \tilde{I}(R_\alpha^2 \nabla^2) - \frac{2D_r k}{g\rho} \right] f_k(\mathbf{r}, t), \quad (\text{A14})$$

where  $\tilde{I}(R_\alpha^2 \nabla^2)$  represents a pseudo-differential operator that is defined by the power series Eq. (A13).

The equally weighted summation over orientational interactions with particles in an isotropic neighborhood of radius  $R_\alpha$  corresponds to an interaction kernel  $\hat{I}(r) = \Theta(r - R_\alpha)$  in Eq. (A1). The Fourier-transform of the appropriately normalized kernel  $I(r) = \hat{I}(r)/(2\pi R_\alpha^2)$  defined by Eq. (A3) then reads

$$\tilde{I}(x) = \frac{2J_1(x)}{x}, \quad (\text{A15})$$

where  $J_1$  denotes the Bessel function of the first kind (Fig. S1).

To map the coarse-grained mode dynamics Eq. (A12) for  $k$ -atic alignment interactions ( $g > 0$ ) to the GL as a mean-field model, we consider the Taylor series of  $\tilde{I}(x)$  given in Eq. (A15) around  $x = 0$ , which implies a non-vanishing coefficient  $\beta_1 = -1/8$  in Eq. (A13) and is accurate to  $\mathcal{O}(x^4)$ . Using this expansion for the operator in Eq. (A14) leads to Eq. (12) and allows for the identification of an effective mean-field correlation length  $L$  in terms of the microscopic interaction radius  $R_\alpha$  [Eq. (13)].

To connect Eq. (A12) to the SH equation as a mean-field description of anti-aligning  $k$ -atics ( $g < 0$ ), we first

note that, for  $|g|\rho \gg 1$ , we can identify  $\lambda(q) = -\tilde{I}(q)$  as the dispersion relation that describes the stability ( $\lambda < 0$ ) or instability ( $\lambda > 0$ ) of homogeneous states under perturbations with wavelength  $2\pi/q$ . Consequently, the first interval in which the Fourier-space representation of the interaction kernel (Fig. S1, solid line) changes its sign indicates a band of unstable wave vectors. Because this sign-change is not captured by the Taylor series of  $\tilde{I}(x)$  up to fourth order around  $x = 0$ , we instead empirically define an approximation  $\bar{\lambda}$  such that *i*)  $\bar{\lambda}(q) = \lambda(-q)$  and  $\bar{\lambda}(0) = 1$ , and *ii*) the smallest unstable wave-vector and the most unstable wave-vector are approximately the same for  $\bar{\lambda}(q)$  and  $\lambda(q)$  (Fig. S1, dashed line). With this approximation, Eq. (A12) implies the real-space representation Eq. (20) for the linearized mode dynamics and a length-scale matching as given in Eq. (22).

Finally, we note that a generalization of the hierarchy of mode Eqs. (A6) to the case of finite-range interaction kernels still allows to decouple the dynamics of modes  $n = jk$  for arbitrary integer  $j$  from all other modes with  $n \neq jk$ . However, the closure assumptions described in Appendix A 1 lead in this case to additional nonlinear terms in the final dynamic equation of the mode  $f_k$ . These terms, which are  $\mathcal{O}(f_k^2 \nabla^2 f_k)$  to lowest order, have for simplicity been neglected in Eqs. (12) and (20).

## Appendix B: Landau-de Gennes (LdG) theory of DLCs with $k$ -fold symmetry

We first explain how the LdG theory of nematic liquid crystals can be naturally generalized to describe DLCs with arbitrary  $k$ -fold symmetries. Subsequently, we will formally map the resulting relaxation dynamics onto the mean-field Eq. (1) and discuss simple fractional defect solutions in free space. To this end, we focus on aligning interactions corresponding to  $\mathcal{L} = L^2 \nabla^2$  in Eq. (1); the anti-aligning case can be treated in the same manner [66].

### 1. Free energy of $k$ -atic DLCs in 2D

Properties of DLCs can be conveniently studied using appropriate free-energy functionals. Typically, these functionals are constructed using vector and tensor-valued fields to encode the underlying microscopic symmetries. Classic examples of this approach are the Frank free energy [57] for polar liquid crystals ( $k = 1$ ) and LdG free energy [1] for nematics ( $k = 2$ ) that are formulated in terms of vectors and traceless symmetric (nematic) tensors, respectively. A particular advantage of this formulation is that a free energy can be systematically constructed as an expansion in terms of the available scalar (rotationally invariant) contractions that can be formed by the given tensorial objects.

A generalization of this approach to arbitrary  $k$ -fold symmetric systems can be realized using traceless symmetric tensors of rank  $k$ , denoted by  $Q_{i_1 \dots i_k}^{(k)}$ , which are

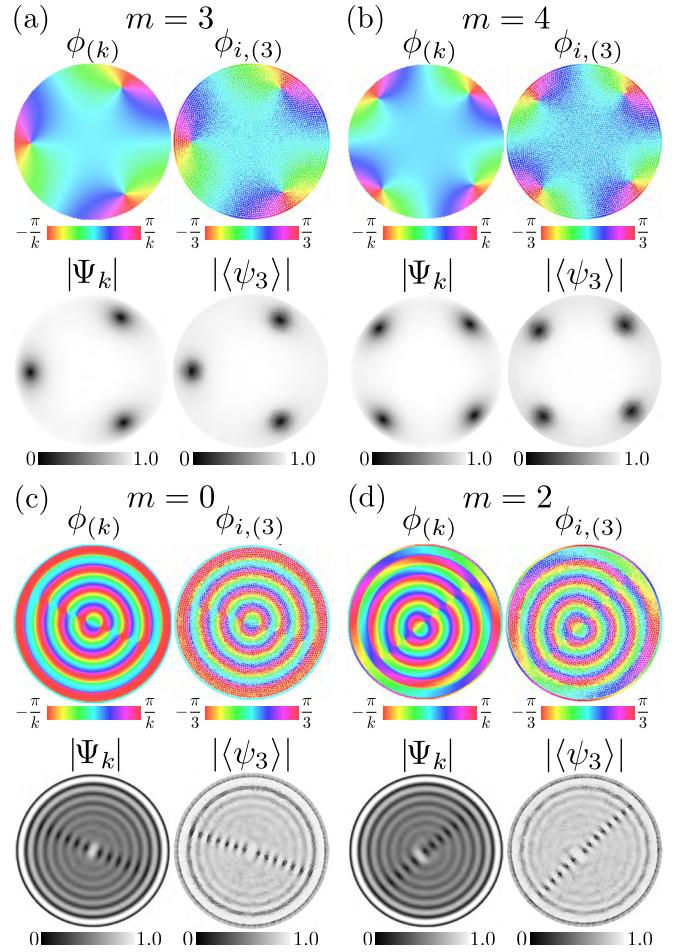


FIG. S2. Additional stationary and long-lived solutions of the generalized GL Eq. (1) and particle model Eq. (6) on a unit disk. (a) Stationary solutions emerging from random initial conditions in the generalized GL Eq. (1) with  $\mathcal{L} = L^2 \nabla^2$  (left) and in particle simulations with aligning interactions (right) for boundary anchoring Eq. (14) with  $\gamma_k = \theta$  and  $m = 3$ . All other parameters as in Fig. 2c,d. (b) Same as (a) for boundary anchoring with  $m = 4$ . (c) Stationary solutions of the generalized GL Eq. (1) with  $\mathcal{L} = -L_1^2 \nabla^2 - L_2^2 (\nabla^2)^2$  (random initial conditions, left) and long-lived solutions in the particle model with anti-aligning interactions (right) for boundary anchoring Eq. (14) with  $m = 0$ . All other parameters as in Fig. 4a. Initial director orientation in particle simulations were sampled from stationary textures solution of the SH equation and evolved according to Eq. (6) until  $D_\tau t = 500$ . (d) Same as (c) for boundary anchoring with  $m = 2$ .

invariant under rotations of  $2\pi/k$ . To connect a description of  $k$ -atic systems in terms of such  $k$ -atic tensors to Eq. (1), we start from the generic free energy

$$F_{(k)} = \sigma \int dA \left[ f(Q_{(k)}) + \frac{L^2}{2} \left( \partial_j Q_{i_1 \dots i_k}^{(k)} \right)^2 \right], \quad (\text{B1})$$

where  $\sigma$  and  $L$  are parameters describing the  $k$ -atic system, and the function  $f(Q_{(k)})$  depends on rotational invariants of the  $k$ -atic tensor. In Eq. (B1) the role of  $L$  as an effective bending rigidity of the local  $k$ -atic field

becomes explicit.

Because  $k$ -atic tensors in two dimensions have only two independent degrees of freedom for any  $k$ , there exists only one rotational invariant

$$Q_{(k)} = \sqrt{2^{1-k} Q_{i_1 \dots i_k}^{(k)} Q_{i_1 \dots i_k}^{(k)}}, \quad (\text{B2})$$

which can be identified as the local  $k$ -atic order. The remaining degree of freedom can then be chosen as the local orientation of the  $k$ -atic director  $\phi_{(k)} \in (-\frac{\pi}{k}, \frac{\pi}{k}]$ . Adopting this local parametrization,  $k$ -atic tensors  $Q_{i_1 \dots i_k}^{(k)}$  are uniquely determined by specifying the two tensor components

$$a_k := Q_{x \dots x x}^{(k)} = Q_{(k)} \cos k\phi_{(k)}, \quad (\text{B3a})$$

$$b_k := Q_{x \dots x y}^{(k)} = Q_{(k)} \sin k\phi_{(k)}, \quad (\text{B3b})$$

with all other components being implied by the index symmetry and tracelessness.

To determine a minimal form of the function  $f(Q_{(k)})$  in Eq. (B1) that is allowed by the underlying symmetries, one has to analyze the possible contractions between  $k$ -atic tensors that can be constructed to form scalars. Using the properties of general  $k$ -atic tensors, one can show that cubic contractions between  $k$ -atic tensors must vanish for arbitrary  $k$  – a fact that is well-known for nematics  $k = 2$ . Hence, a minimal LdG expansion for  $f(Q_{(k)})$  in the free energy (B1) is, for any  $k$ , given by

$$f = \frac{A}{2} Q_{(k)}^2 + \frac{B}{4} Q_{(k)}^4, \quad (\text{B4})$$

where  $A \in \mathbb{R}$  and  $B > 0$  are constant material parameters. The relaxation dynamics

$$\partial_t Q_{i_1 \dots i_k}^{(k)} = -\gamma^{-1} \delta F_{(k)} / \delta Q_{i_1 \dots i_k}^{(k)}$$

with rotational viscosity  $\gamma$  thus takes the form

$$\tau \partial_t Q_{i_1 \dots i_k}^{(k)} = - \left( A + B Q_{(k)}^2 \right) Q_{i_1 \dots i_k}^{(k)} + L^2 \nabla^2 Q_{i_1 \dots i_k}^{(k)}, \quad (\text{B5})$$

where  $\tau = \gamma/\sigma$ . Finally, the tensor parameterization given in Eqs. (B3) can be used to define the complex  $k$ -atic order parameter

$$\Psi_k = a_k + i b_k. \quad (\text{B6})$$

This definition is equivalent to  $\Psi_k$  given in Eq. (3) and explicitly relates the magnitude  $|\Psi_k| = Q_{(k)}$  of  $k$ -atic order and the  $k$ -atic phase  $\phi_{(k)}$  as introduced in Eq. (4) to a representation of  $k$ -atic DLCs in terms of traceless symmetric tensors of rank  $k$ . With this, the relaxation dynamics Eq. (B5) yields Eq. (1) with  $\mathcal{L} = L^2 \nabla^2$ , corresponding to a ‘real’ GL equation.

## 2. Fractional point defect solutions in free space

The simplest scenario to study fractional defects in the GL equation, or equivalently in Eq. (B5), is to consider a

limit  $B = -A \rightarrow \infty$ , such that  $|\Psi_k| = \sqrt{-A/B} = 1$  and the system resides in a perfectly ordered state. Stationary solutions are then determined by

$$\nabla^2 \phi_{(k)} = 0. \quad (\text{B7})$$

The regularity of the complex order parameter  $\Psi_k$  away from the defect demands  $k[\phi_{(k)}(r, \theta + 2\pi) - \phi_{(k)}(r, \theta)] = 2\pi m$  for any integer  $m$ , where  $(r, \theta)$  denote cylindrical coordinates. Hence, physically permissible topological defect solutions of Eq. (B7) can be written as

$$\phi_{(k),m}(\theta) = \frac{1}{k} \arg(e^{im\theta}), \quad (\text{B8})$$

which provides an example for a fractional defect state with topological charge  $m/k$  as defined by Eq. (5).

For finite values of  $A$  and  $B$ , the scaling behavior close to and far away from  $m/k$ -defects can be obtained by following the approach of Ref. [67]. Using an ansatz  $\Psi_k = Q_0(r) \exp[ik\phi_{(k)}(\theta)]$  in the GL, one again finds stationary fractional  $m/k$ -defect solutions Eq. (B8), where the magnitude  $Q_0(r)$  is now a function of the distance  $r$  from the defect center. In the  $k$ -atically ordered regime  $A < 0$ , the magnitude increases near the defect ( $r \ll L$ ) as  $Q_0 \sim (r/L)^m$  and converges far away from the defect ( $r \gg L$ ) to the value  $\sqrt{-A/B}$  with an asymptotic scaling behavior of  $Q_0 \sim 1 - (mL)^2/(2|A|r^2)$ .

## Appendix C: Swift-Hohenberg equation

In this appendix, we provide additional insights into the connection between the SH equation for anti-aligning interactions, corresponding to  $\mathcal{L} = -L_1^2 \nabla^2 - L_2^4 (\nabla^2)^2$  in Eq. (1), and the  $k$ -atic particle model and motivate the definition of the phase-chirality parameter given in Eq. (23).

### 1. Patterns on periodic domains

To explore the relation between the SH model and the  $k$ -atic particle model with anti-alignment in more detail, we have studied the spontaneous pattern formation of both models on a periodic unit square using numerical simulations (Fig. S3). In both models and for the parameter regime studied in this work, many different texture patterns spontaneously form. These patterns can be broadly grouped in defect-free wave-like (Fig. S3a,c) and checkerboard-like patterns (Fig. S3b,d), where the latter represent  $\pm 1/k$ -defect-lattices with vanishing total topological charge that are clearly visible in the order parameter magnitudes. Furthermore, we note that a stationary texture pattern that occurs in the SH model is – for all cases that were tested – also stationary in the particle model, if the microscopic directors are initialized with the corresponding  $k$ -atic phase field. The opposite

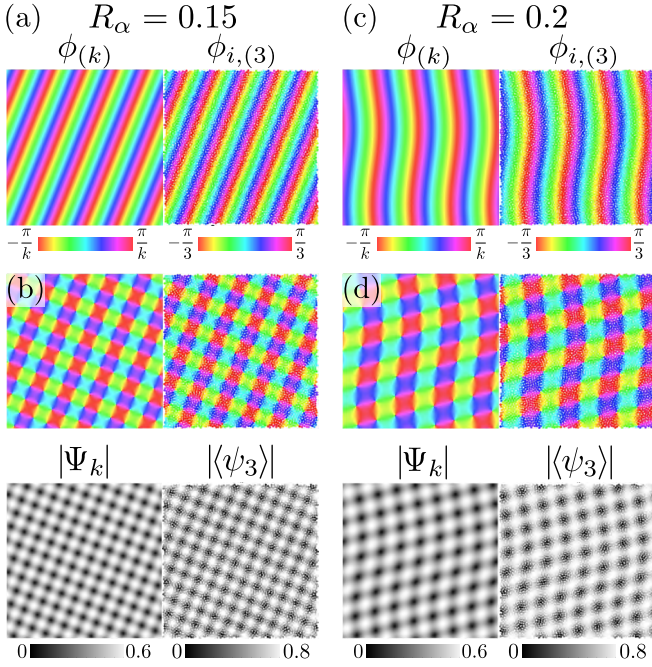


FIG. S3. Spontaneous pattern formation in the SH Eq. (1) with  $\mathcal{L} = -L_1^2 \nabla^2 - L_2^4 (\nabla^2)^2$  and in the particle model with anti-alignment interactions [Eq. (6) with  $g < 0$ ; 5,000 particles] on a unit square with periodic boundaries. (a) Example of a defect-free wave-like texture pattern that can be found in both models. (b) Example of a checkerboard-like texture pattern (same color code as in a) that contains a  $\pm 1/k$ -defect-lattice visible in the magnitude of the  $k$ -atic order parameter  $|\Psi_k|$  and in the temporal average  $\langle \cdot \rangle$  of the magnitude of the microscopic 3-atic order parameter  $\psi_3 = \sum_{j \in \mathcal{N}_i} \exp(3i\alpha_j) / |\mathcal{N}_i|$ . (c,d) Similar patterns for a different microscopic interaction radius and an accordingly modified SH equation. Parameters:  $A = 1$ ,  $B = 1$ ,  $L_1 = 0.305R_\alpha$  and  $L_2 = 0.205R_\alpha$  (SH equation) and  $k = 3$ ,  $g = -1$ , and  $D_r = 1$  (particle model).

is not true: The particle dynamics sometimes gets stuck in long-lived irregular patterns that are not stationary when used in the SH equation.

## 2. Phase-chirality parameter

To motivate the definition the phase-chirality parameter given in Eq. (23), we note that the gradient of the phase of any complex number  $|z|e^{i\phi} = a(x, y) + ib(x, y)$  can be expressed as

$$\partial_x \phi = \frac{a \partial_x b - b \partial_x a}{|z|^2}, \quad (\text{C1})$$

and  $\partial_y \phi$  has the same form. This expression diverges at defects or defect-lines where  $|z| = 0$ . Hence, we consider the regularized phase-chirality parameter  $\Phi_c$  defined in Eq. (23) to capture chiral signatures in the phase textures of steady state solutions  $\Psi_k$ .

## Appendix D: Numerical simulations

In the following, we discuss the coefficient matching and comparison of relaxation time scales between mean-field model and microscopic simulations. Finally, we summarize details of the different methods and workflows that have been used to generate the numerical results presented in this work. Furthermore,

### 1. Matching homogeneous mean-field coefficients with parameters of the microscopic model

To match the homogeneous coefficients  $A$  and  $B$  in Eq. (1) to the microscopic dynamics, we note that the latter was considered in a regime of high particle density, viz.  $D_r / (|g|\rho) \ll 1$ . In this case, Eq. (11) implies  $\bar{A} \approx -1$  for aligning interactions ( $g > 0$ ) and  $\bar{A} \approx 1$  for anti-aligning interactions ( $g < 0$ ). Accordingly, we have throughout this work set  $A = -1$  for simulations of the GL equation [Eq. (1) with  $\mathcal{L} = L^2 \nabla^2$ ] and  $A = 1$  for simulations of the SH equation [Eq. (1) with  $\mathcal{L} = -L_1^2 \nabla^2 - L_2^4 (\nabla^2)^2$ ]. The coefficient  $B$  was set empirically: Away from defects, we expect  $|\Psi_k| \simeq |\psi_k| \approx 1$  for an ordered state in the microscopic model, which is ensured in the GL equation by setting  $B = 1$ . The same value is adopted in simulations of the SH equation, where it also leads to good agreement with order parameter magnitudes of the microscopic model with  $g < 0$ .

### 2. Comparison of characteristic time scales

The relaxation time scale introduced with the generalized GL Eq. (1) is given by  $\tau$ . From the coarse-graining result Eq. (10), we expect  $\tau$  to be comparable to the time scale  $\bar{\tau} = 2 / (|g|k\rho)$  if the mean-field parameters and operators  $\mathcal{L}$  are matched according to Eqs. (11), (13) and (22). To test this, we have to compare observations from a dynamic process as described by the generalized GL Eq. (1) and by the microscopic model Eq. (6). To this end, we refer to the defect relaxation dynamics depicted in Fig. 2c,d, where the time points of snapshots of the ‘real’ GL equation simulation in units of  $\tau$  are provided in the caption. The time scale of particle simulations was set for practical reasons by the inverse rotational diffusion constant  $1/D_r$ , i.e. in units of  $\bar{\tau}$  it was given by  $s\bar{\tau}$  with

$$s = \frac{2D_r}{|g|k\rho}. \quad (\text{D1})$$

Scaling numerical time points of particle simulations for the given parameters accordingly ( $g = 0.25$ ,  $k = 3$ ,  $\rho = 4000/\pi$ ,  $D_r = 1$ ) then leads to the temporal coordinates  $t/\bar{\tau}$  of the particle model snapshots listed in the caption of Fig. 2d. These snapshots were chosen such that they best resemble textures from the mean-field model. From the relative values of corresponding

time points, we can estimate  $\bar{\tau}/\tau \approx 0.4$ , indicating that the coarse-graining predicts a slightly faster relaxation dynamics than actually exhibited by the matched mean-field model Eq. (1).

### 3. Numerical methods: Mean-field simulations

Real and imaginary part of the GL Eq. (1) with  $\mathcal{L} = L^2 \nabla^2$  were simulated separately on the unit disk using the finite element partial differential equation solver provided by Matlab [68]. Boundary anchoring profiles described in Eq. (14) were imposed as Dirichlet boundary conditions.

For the case of the SH equation, Eq. (1) with  $\mathcal{L} = -L_1^2 \nabla^2 - L_2^4 (\nabla^2)^2$  was rewritten as a system of two pairs of second order differential equations and  $\nabla^2 \Psi_k|_{\partial S} = 0$  was included as an additional boundary condition. The open-source Dedalus framework [69] was used to spectrally solve the SH equation on a periodic domain with  $256 \times 256$  grid points using a Fourier-basis and integration time steps of  $dt = 10^{-2}$  in units of  $\tau$ .

### 4. Numerical methods: Microscopic model

Bulk particles were first randomly positioned on the respective domain (a unit disk or a square with periodic boundary). For simulations on the unit disk, a single line of boundary particles with fixed positions was additionally placed along the outline of the disk. In the next step, the bulk particles were left to distribute themselves homogeneously in space in the absence of noise via

a pair-wise repulsive force  $\mathbf{f} \sim \nabla \exp(-r_p^2/L_f^2)$ , where  $L_f^2 = A/N$  for  $N$  particles distributed on a domain of area  $A$ . After that, all particle positions were kept fixed and Eq. (6) was integrated using the Euler-Maruyama method [70] with integration time steps of  $dt = 10^{-4}$  in units of  $1/D_r$ . To realize the boundary anchoring on the unit disk, boundary particles did not participate in the stochastic dynamics but kept the fixed director angle profile given in Eq. (17) and acted as neighbors for the director dynamics of bulk particles.

### 5. Initial conditions

Random initial conditions have been used for most of the shown simulation results, except for the time series in Fig. 2c,d, as well as to generate steady state pattern Fig. 4a ( $m = 0$ ) and the initial state  $t = 0$  in Fig. 5 ( $m = 2$ ). To describe the initial conditions for the latter cases, we denote in the following  $(r, \theta)$  and  $(r_i, \theta_i)$  as the position of a given field or particle position in cylindrical coordinates. The initial point defect states in Fig. 2c,d ( $t = 0$ ) are respectively given by  $\Psi_k = e^{i2\theta}$  and  $\alpha_i = (2/3)\theta_i$  ( $k = 3$  in the particle model), which maps to the  $k$ -atic phase angles  $\phi_{(k)}$  and  $\phi_{(k),i}$  as shown in Eqs. (15) and (16). To generate spiral stationary states that do not form spontaneously, we use  $h_m(r, \theta) = 8\pi(r - 1) + m\theta$ , and initialize the order parameter field as  $\Psi_k = e^{ih_m(r, \theta)}$  and the particle director field as  $\alpha_i = [h_m(r_i, \theta_i)/3 \bmod 2\pi]$  ( $k = 3$  in the particle model). The equilibration of these states gives rise to the patterns shown in Fig. 4a ( $m = 0$ ) and to the initial state  $t = 0$  in Fig. 5 ( $m = 2$ ).